A00-16425

AIAA 2000-0548

Microactuator Arrays for Sublayer Control in Turbulent Boundary Layers Using the Electrokinetic Principle

Francisco J. Diez-Garias and Werner J.A. Dahm

Laboratory for Turbulence & Combustion (LTC)
Department of Aerospace Engineering
The University of Michigan

Phillip H. Paul

Microtechnology Division 8355
Sandia National Laboratories

38th Aerospace Sciences Meeting & Exhibit
10-13 January 2000 / Reno, NV

AIAA Paper No. 2000-0548 to be presented at the 38th AIAA Aerospace Sciences Meeting, January 10-13, 2000, Reno, NV

Microactuator Arrays for Sublayer Control in Turbulent Boundary Layers Using the Electrokinetic Principle

Werner J.A. Dahm[1] and Francisco J. Diez-Garias[2]

Laboratory for Turbulence and Combustion (LTC)
Department of Aerospace Engineering
The University of Michigan
Ann Arbor, MI 48109-2140

Phillip H. Paul[3]

MicroTechnology Department 8355
Sandia National Laboratories
Livermore, CA 94550

Control principles and microactuator arrays are described for drag reduction in turbulent boundary layers by manipulation of streamwise sublayer vortical structures. The microactuators described here are fundamentally different from traditional MEMS approaches. They have no moving parts, and induce volume displacements of the sublayer vortices by means of electrokinetic pumping under a time-varying applied voltage. Such electrokinetic microactuators have characteristics making them potentially suited for practical sublayer control on real vehicles. Theoretical frequency response of such electrokinetic microactuators is in the MHz range; actual microactuators have been fabricated and tested to frequencies as high as 20 kHz and shown essentially no AC performance losses. A basic three-layer design for such electrokinetic microactuator arrays has been developed, and several generations of microactuator arrays have been fabricated. Current fabrication is based on laser drilling of electrokinetic channels in plastic substrates with traditional metallization processes for the electrodes and leadouts. A porous polymer matrix is used for the electrokinetic channels. Two types of microactuator arrays are described; "point" actuators for active control with colocated sensors and processing, and "slot" actuators for passive control based on the "oscillating wall" approach, for which no local sensors or processing are required.

1. INTRODUCTION

Control of vehicle aerodynamics is among the highest-impact applications of microsystems technology for military and commercial purposes. A reduction in the drag on an air vehicle of just a few percent translates into enormous system-wide reductions in fuel weight and operating costs, and corresponding increases in vehicle range and payload delivery. Similarly, actuator systems capable of on-demand vortex generation over delta wings, strakes, and other control surfaces in fighter aircraft would permit dramatic increases in maneuverability, and large reductions in radar cross-section through elimination of traditional control surfaces. Such benefits of microsystems-based flow control extend to naval surface and undersea vehicles as well, including ships, submarines, and torpedoes, as well as to unmanned vehicles used in a variety of applications such as UAV's and MAV's. Similar technologies would also find use in a wide range of other flow control situations involved in propulsion systems, spanning from control of mixing in advanced gas turbine combustors, to active control of surge and stall in compressors.

The prospects of actually achieving such revolutionary advances in flow control are far more realistic than they might at first seem. In the realm of vehicle control, the underlying physics of the problem at hand and the inherent characteristics of a microsystems-based approach are ideally matched. The thin boundary layer that exists directly adjacent to the surface of any practical vehicle is one of the most powerful nonlinear systems found in nature, capable of amplifying the effect of small microactuator-induced perturbations into very large changes in the aerodynamic forces and moments acting on the vehicle. Moreover, the inherent problem of matching the length and time scales between microactuators and the physical problem at hand makes the viscous sublayer of a turbulent boundary layer a natural choice for microsystems-based control. The exceedingly small length scales associated with flow structures that are naturally present in the sublayer are ideally matched to microscale actuators. However the high performance required for sublayer control places rather stringent limits on the types of actuators that may be suitable for this task.

One approach for controlling the vehicle boundary layer is to exploit the streak-like vortical structures that exist naturally in the viscous sublayer. These sublayer vortices may be as small as 10 μm thick, spaced about 100 μm apart and roughly 1 mm long, and advect past any fixed point at frequencies up to 10-100 kHz. MEMS sensor technologies currently exist that are capable of detecting these vortical structures in the viscous sublayer via their wall shear stress signature. Indeed, detection of high-speed sublayer streaks in turbulent boundary layers has been demonstrated in relatively low-speed wind tunnel tests. A variety of sensors are available today that can accomplish this task, including micro hot-wire anemometers, micro surface shear stress balances, and micro pressure sensors. Extensive reviews of prior related work can be found in the literature (*e.g.*, Bushnell & McGinley 1989; Fiedler & Fernholz 1990;

---

1. Professor; AIAA Senior Member; Corresponding author.
2. Graduate Student; AIAA Student Member.
3. Technical Staff; AIAA Member.

Wilkinson 1990; Gad-el-Hak 1989, 1994, 1996); McMichael 1996; Ho & Tai 1996, 1998; Pollard 1998; Lumley & Blossey 1998; Löfdahl & Gad-el-Hak 1999).

Moreover, the control algorithms and associated processing electronics necessary to couple these sensors to an appropriate set of microactuators are also in reasonably good shape. The required algorithms and processing capabilities are not very far beyond what has already been demonstrated in a number of less demanding low-speed wind tunnel tests. In fact, reduction of surface shear stress has been successfully demonstrated with remarkably simple control algorithms in a number of laboratory-scale flows (*e.g.*, Breuer et al 1989, Moin & Bewley 1994, Jacobsen & Reynolds 1998).

However, suitable microactuators for practical vehicle sublayer control have been lacking to date. Although there are a broad range of microactuators available today, based on a wide variety of different operating principles, these generally do not meet the stringent requirements noted above for practical boundary layer control on real vehicles. In this paper paper, we describe the first use of the electrokinetic principle (*e.g.*, Potter 1961) as the basis for an entirely new class of microactuators for integration in large arrays to meet the requirements for sublayer control in turbulent boundary layers on vehicles (Dahm et al 1997).

2. Review of Sublayer Vortical Structure

Turbulent boundary layers obey a universal structure and scaling under so-called "equilibrium" conditions, which typically apply over the vast majority of a vehicle surface. This makes it possible to approach the problem of vehicle control with a general set of microactuator arrays, rather than having to resort to a separate approach for each vehicle type. It is necessary to be aware of at least the basics of this general structure and its scaling in order to understand the approach being taken here, and to understand the performance requirements that they dictate for microactuator arrays. In this section, we review certain key aspects of the structure and dynamics of equilibrium turbulent boundary layers.

The central issue concerns the form of the mean velocity profile $u(y)$ with increasing distance y from the vehicle surface (referred to generically as the "wall", located at $y \equiv 0$). There are two distinct mechanisms that contribute to momentum transport from the wall to the fluid and then within the fluid above the wall. The first is classical molecular diffusion, with the momentum diffusivity being the "kinematic viscosity" ν, and the second is turbulent transport by velocity fluctuations in the flow itself. Directly at the wall, the fluid cannot move and thus the turbulent transport there must vanish. Consequently for a small distance above the wall the turbulent transport must therefore remain essentially negligible. For this reason, there is a layer of fluid adjacent to the wall within which molecular transport far exceeds turbulent transport. With increasing distance from the wall, the momentum flux density due to molecular transport must remain roughly constant, while that due to turbulent transport increases, and thus turbulent transport eventually becomes the dominant mechanism. The boundary layer therefore naturally has a two-layer structure – an "inner layer" directly adjacent to the wall within which molecular transport dominates, and an "outer layer" within which turbulent transport dominates. The crossover between these two transport mechanisms occurs in the outer part of the inner layer and the inner part of the outer layer – called the "log layer" for reasons that will become evident below.

Within the inner layer, owing to the dominance of diffusion the momentum flux density must be roughly constant at a value called the "wall shear stress" τ_w, literally the value of the shear stress at the wall. All processes within this layer are assumed to be properly scaled with this wall shear stress, with the viscosity ν, with the fluid density ρ, and with the distance y above the wall. It is convenient to express such near-wall scalings in terms of the characteristic velocity defined from these quantities, namely $u_\tau \equiv (\tau_w/\rho)^{1/2}$, often called the "friction velocity", and the characteristic length $l_\tau \equiv \nu/u_\tau$ termed the "wall unit". The appropriately scaled velocity profile is then $u^+(y^+)$, where $u^+ \equiv u/u_\tau$ and $y^+ \equiv y/l_\tau$. The velocity profile throughout the inner layer, when scaled in this manner, is universal for *all* equilibrium turbulent boundary layers.

Within the outer layer, however, the velocity profile is not entirely universal, and varies somewhat depending on the local boundary layer thickness δ and on the local streamwise pressure gradient dp/dx. The latter is determined via the Bernoulli equation by the local acceleration of the fluid outside the boundary layer as it negotiates around the vehicle shape. Thus irrespective of the particular vehicle, the outer layer structure (under equilibrium conditions) can be cataloged in terms of an appropriately scaled pressure gradient parameter Π. Various ways of expressing this scaling have been proposed, with the most successful being the "law of the wake" (Coles 1956). In the overlap region, namely the inner part of the outer layer and the outer part of the inner layer, the velocity profile must become independent of the pressure gradient, and this turns out to demand that the velocity profile in this overlap region must have a logarithmic form – hence the term "log layer". The remainder of the outer layer is referred to as the "defect layer", because its shape is described in terms of the departure (or defect) it demonstrates in relation to the shape that would result if the logarithmic scaling continued there.

Excluding the log layer, the inner layer extends to about $y^+ \approx 30$, with the region from $0 < y^+ < 10$ termed the "viscous sublayer", and the remainder called the "buffer layer". Thus the viscous sublayer is about 10 wall units thick, and the inner layer up to the log layer is about 30 wall units thick. The physical thicknesses that these correspond to depend on the value of l_τ, and hence on the wall shear stress (and thus on the boundary layer thickness δ and pressure gradient parameter Π), the fluid density, and the viscosity. These vary depending on the vehicle size, its speed, and the fluid through which it moves.

Owing to the dominance of diffusive transport very close to the wall the vorticity there must be uniform, and hence the velocity must increase linearly with distance from the wall. Within the viscous sublayer (*i.e.*, below $y^+ \approx 10$), the form of $u^+(y^+)$ must thus simply be $u^+ = y^+$. This linear velocity profile remains steady until the resulting uniform vorticity layer adjacent to the wall reaches a thickness at which it becomes unstable; this forms the lower edge of the buffer layer. At this distance from the wall, naturally-occurring infinitesimal disturbances cause the otherwise uniform vorticity layer to develop sinusoidal instabilities along the spanwise (cross-stream) direction, denoted z. Amplification and nonlinear growth of this spanwise instability leads to the formation of elongated concentrations of vorticity oriented along the streamwise direction, denoted x. The resulting streamwise vortical structures at the outer edge of the viscous sublayer have a spacing, in the scaled spanwise coordinate $z^+ \equiv z/l_\tau$, of about $z^+ \approx 100$. The length of these "sublayer vortices" in the scaled streamwise coordinate $x^+ \equiv x/l_\tau$ is typically about $x^+ \approx 1000$, but varies from about 400 – 1500. In other words, the sublayer vortices are about 1000 wall units

long, and are spaced about 100 wall units apart. Since the vortices are located roughly 10 wall units above the wall, they will advect at a speed $u^+ \approx 10$, and thus move over any fixed point on the wall with a frequency of about $f^+ \approx 10^{-2}$.

3. Sublayer Control Principles

It is these streamwise vortices at the outer edge of the viscous sublayer that are the key to momentum transport from the wall to the bulk fluid, and hence to the drag that acts on the vehicle. Under the influence of their mutual Biot-Savart induced motion as well as that of their images on the opposite side of the wall, these streamwise vortices must naturally group into pairs having alternating sense of circulation. Each streamwise vortex pair remains nominally steady until the combined induced motion of the two elongated vortices abruptly lifts them away from the near-wall region and into the outer layer, in a process termed "bursting". In doing so, low momentum fluid in the wall-fixed coordinate frame (high momentum fluid in an absolute frame) is transported from the inner layer to the outer layer, at a much greater rate than would be the case by diffusion alone. It is due to this bursting mechanism and the accompanying greatly increased rate of momentum transport from the wall to the fluid that turbulent boundary layers produce far greater drag on a vehicle than do laminar boundary layers.

Interrupting this delicate, nonlinear, Biot-Savart-induced lifting mechanism before bursting occurs has long been an objective in fluid mechanics and aerodynamics. It has been demonstrated, both in laboratory experiments and in numerical simulations, that this can be accomplished by acting on the streamwise vortices in any of a number of ways so as to offset the Biot-Savart induced velocities that lead to the sudden bursting. For the present microactuator arrays (see Fig. 1), the individual actuators serve as point volume sources that displace (either positively or negatively) a fixed volume of fluid between the wall and the inner layer. The motion which this volume source field induces serves to displace the streamwise vortices along the spanwise direction, thereby locally increasing or decreasing the separation between the two elongated vortices in a streamwise vortex pair. This counteracts the Biot-Savart induced motion of the vortices on each other, thus interrupting the bursting process.

As for a closed-loop feedback control approach that drives an array of such individually addressable "point" microactuators, there are roughly speaking two schools of thought regarding the best way to do this. The first, which may be termed the "deterministic" approach, is to use sensors to identify the wall shear stress or wall pressure signature of a pair of streamwise vortices that are about to burst, and then use co-located actuators to manipulate the vortices in such a way as to delay or defeat the bursting process. The second, which might be termed a "stochastic" approach, ignores the detailed dynamics of the bursting process itself and instead uses an artificial intelligence procedure. In that case, a neural network between a group of sensors and actuators is trained over time in such a way as to minimize the wall shear stress (*e.g.*, Choi et al 1994). Both approaches have met with considerable and roughly comparable success in laboratory experiments and in numerical simulations, demonstrating reductions of in the range of 20-30% in the wall shear stress.

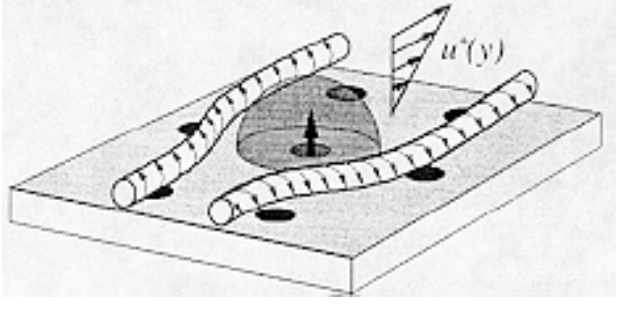

Figure. 1. Notional representation of sublayer vortex displacement by an array of individually addressable microactators designed to produce positive or negative volume flow from the wall into the inner layer. Large arrays of such "point" microactuators would allow drag reductions by interrupting the bursting process associated with Biot-Savart induced interactions between adjacent sublayer vortices.

The scenario outlined above involves *closed-loop* control of the *equilibrium* structure and dynamics of the boundary layer. An alternative uses *open-loop* control of the *nonequilibrium* dynamics in the near-wall region of the boundary layer. This is motivated by experimental and numerical observations showing that, when a boundary layer is subjected to a sudden transverse pressure gradient or crossflow, the flow experiences temporary reductions in its turbulent transport. This suggests that it may be possible to sustain this effect by maintaining the boundary layer in a continual nonequilibrium state. One way this might be done is through spanwise oscillations of the wall relative to the streamwise vortices (*e.g.*, Jung *et al* 1992, Akhavan *et al* 1993, Laadhari *et al* 1994). Experiments and numerical simulations have shown that this does produce significant reductions in turbulent transport and thereby reductions in the wall shear stress of up to 40%. The effectiveness depends on the oscillations frequency, with optimal drag reduction again occurring at $f^+ \approx 10^{-2}$. Moreover such an approach does not require any colocated array of sensors to determine the instantaneous pattern of sublayer vortices, or control logic to discern from this the appropriate set of actuator signals. The only requirement is for an occasional sensor to measure the average wall shear stress, which is needed to properly scale the oscillation frequency to achieve optimal drag reductions. The "oscillating wall" approach thus potentially provides a means for open-loop control of the sublayer vortices, and thus obviates the difficulties associated with colocating large arrays of sensors, actuators, and local processing. In practice, it is the fluid above the wall that would be oscillated by a set of microactuators designed to generate volumetric displacements above the wall and thereby induced oscillatory spanwise motions of the fluid in the inner layer.

4. Microactuator Performance Requirements

The two different types of electrokinetic microactuator arrays, shown schematically in Fig. 2, are being pursued for the two different control approaches noted above. For closed-loop control based on individual point microactuators, Fig. 2*b* shows individually addressable microactuators arranged in a regular array with a characteristic separation matched to the sublayer streak spacing. Each actuator produces locally positive or negative volume displacements over a brief interval, corresponding to local suction or blowing at the wall, to displace the individual sublayer vortices as needed to interrupt the bursting process. The volume displacements are created by electrokinetic pumping within individual microactuator channels in a center layer, as will be described in §5. Key performance requirements involve the microactuator spacing, frequency, and flowrate needed to achieve adequate displacement of individual

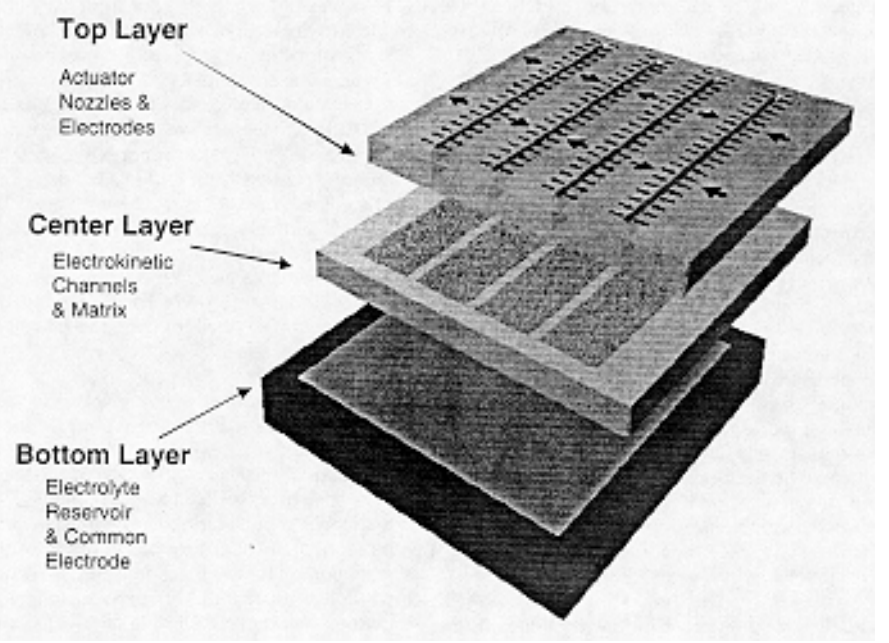

Fig.2*a*. Basic three-layer design of slot-type microactator arrays for "oscillating wall" control approach.

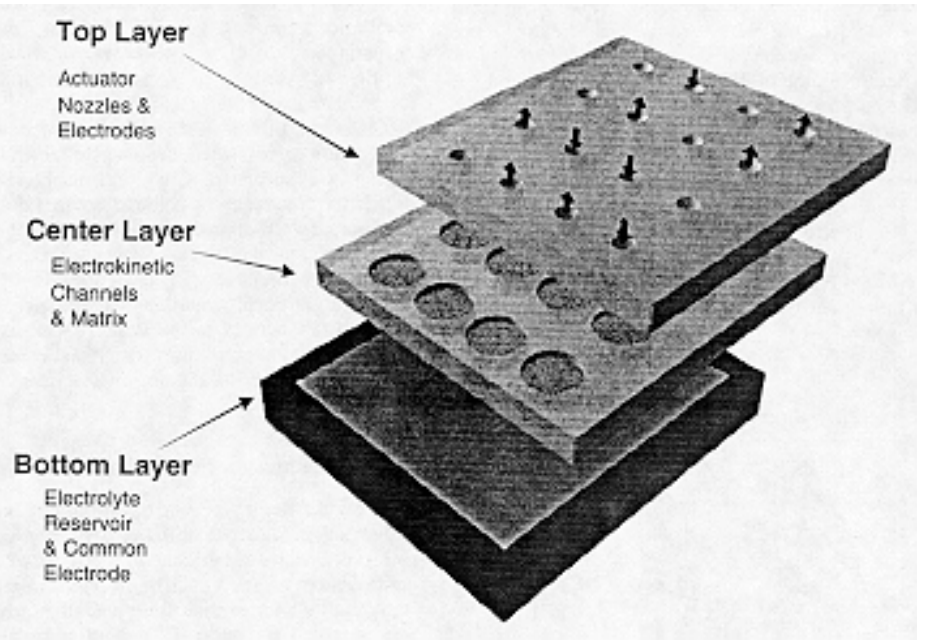

Fig.2*b*. Basic three-layer design of point-type microactator arrays for "traditional" control approach.

Figure 2. Schematics indicating the basic three-layer design for the two types of electrokinetic microactuator arrays being developed. Point microactuators arrays as in Fig. 2*b* are suited for the "traditional" closed-loop control approach based on colocated sensors, processing, and actuators grouped in a basic unit cell. Slot actuator arrays of the type in Fig. 2*a* are suited for the open-loop "oscillating wall" control approach, which eliminates the need for local sensing of the sublayer streaks or control logic to drive the microactuators.

sublayer vortical structures.

For open-loop control based on the oscillating wall approach, volume displacement is through slots nominally aligned with the near-wall flow. Such slot microactuators, shown in Fig. 2*a*, are sized so that many sublayer vortices are typically located between adjacent slot pairs. Adjacent slot pairs produce alternatingly positive or negative volume displacements, in a time-oscillating fashion, to displace fluid above the wall along the cross-stream direction. The volume displacements are again created by electrokinetic pumping within the much larger microactuator channels in a center layer. In this case the slot spacing is less critical, and key performance requirements are the frequency and flowrate needed to achieve effective spanwise oscillation of the fluid above the wall.

Irrespective of the control approach used and the microactuator type it implies, it is necessary to have a set of actuators that can be arranged to allow the streamwise sublayer vortices to be acted upon appropriately. For the closed-loop control approach based on individual point microactuators, based on the forgoing summary of the sublayer vortex structure and dynamics it is apparent that such actuators must be separated by typically 100 wall units, and displace a volume of fluid with an equivalent hemispherical radius of the order of 10 wall units, with a step response that corresponds to a scaled frequency of $f^+ \approx 10^{-2}$. For open-loop control designed around the oscillating wall approach, the actuators must in that case operate effectively at the frequencies demanded by the same $f^+ \approx 10^{-2}$ requirement at which optimal drag reduction is observed.

With this information, it is possible to determine the size and performance requirements to which these conditions correspond for various types of vehicles. These performance requirements will depend on the fluid type (principally air or water, which differ in their density and viscosity), on the vehicle speed, and on the vehicle length. More precisely, the universal structure and scaling of equilibrium turbulent boundary layers shows that the *local* sublayer properties, and hence the *local* microactuator performance requirements, depend on the local boundary layer thickness δ, the local fluid speed U at the "edge" of the boundary layer, the local pressure gradient dp/dx, and the fluid properties. Of these, the direct effect of the pressure gradient is relatively weak; it is the indirect effect of the pressure gradient on the boundary layer thickness δ that dominates. This permits an analysis for each vehicle type without requiring a detailed boundary layer calculation for a specific vehicle geometry. In effect, the performance requirements can be obtained at any streamwise position on the vehicle for a variety of pressure gradient parameters Π ranging from strongly favorable to moderately adverse.

Vehicle class	*Length (m)*	*Speed (m/s)*
Transport aircraft (wing)	3	200
Supersonic fighter (wing)	5	300
UAV (wing)	1	30
Naval surface ship (hull)	180	30
Submarine (hull)	170	10
Torpedo	5	10
Automobile (body)	2	30

Table 1. Sizes and speeds for vehicle classes shown in Fig. 3. For each vehicle type, sublayer control requirements were calculated for several locations x/L and pressure gradient parameters Π for either air or water properties.

Accordingly, Fig. 3*a* shows the results obtained for the required point microactuator spacing and frequency response at four downstream locations (x/L = 0.25, 0.5, 0.75 and 1.0) and for four different pressure gradients. Vehicles for which results are shown in this figure are summarized in Table 1. It is apparent, both from the results shown and from fundamental considerations, that vehicle speed is the principal factor that drives both the spacing and frequency requirements. These requirements are relatively benign for the UAV application, where actuator spacings of several millimeters and step response of 100 Hz are sufficient to act on virtually every sublayer streak. At the other extreme, the supersonic fighter and transport aircraft require actuator spacings of 100 - 200 μm and step response of 10-90 kHz. The various hydronautical applications (which differ from the other cases due principally to the higher fluid density) require microactuator spacings around 300 μm but frequencies of only about 1 kHz. Figure 3*b* gives the equivalent DC volume flow rate requirements for each of these vehicle types. For hydronautical applications, the equivalent DC flow rates required are in the range of 10 μl/min.

These frequency and flowrate requirements represent what is needed to act on essentially every streamwise vortical sublayer structure in the turbulent boundary layer. While the actuator spacing requirements are inflexible, adequate control may be possible with somewhat lower frequency performance. This would involve acting on some, but not all, of the vortical structures. In fact, it is only necessary to act on those structures that are at the point of "incipient bursting", since it is this vortex bursting phenomenon that the microactuators are intended to suppress.

The small actuator spacings required for sublayer control on real vehicles implies that large dense arrays of microactuators must be used to cover key parts of the vehicle surface, as indicated in Fig. 4. However, the local nature of the sublayer vortex dynamics and bursting process suggests that large tiles of such arrays can be composed of much smaller independent unit cells, each with their own sensors, control processing, and actuators. Fundamental considerations suggest that these will consist of a typically 6×6 array of microsensors and microactuators. This local nature of the problem greatly simplifies the sublayer control of turbulent boundary layers.

5. Electrokinetic Microactuator Principles

Electrokinetic fluid microactuators work on the electrokinetic effect (*e.g.*, Potter 1961), discovered in 1807. In macroscale applications, this effect is used in a very wide range of devices and processes. The present study is the first attempt to exploit its potential advantages as the basis for a class of microscale actuators suitable for boundary layer control on vehicles.

Briefly, electrokinetic processes operate by means of a double-layer of ions that forms at an interface, in this case between a solid channel material and an electrolytic fluid. The double-layer thickness in the electrolyte is set by the Debye length, which is typically only 10 - 100 nm. The inner layer contains immobile ions attracted to the charge distribution on the wall, and is at most a few ionic radii thick. The outer layer is much thicker and contains the remainder of the ions, which are free to move. When a potential difference is applied along the channel, the

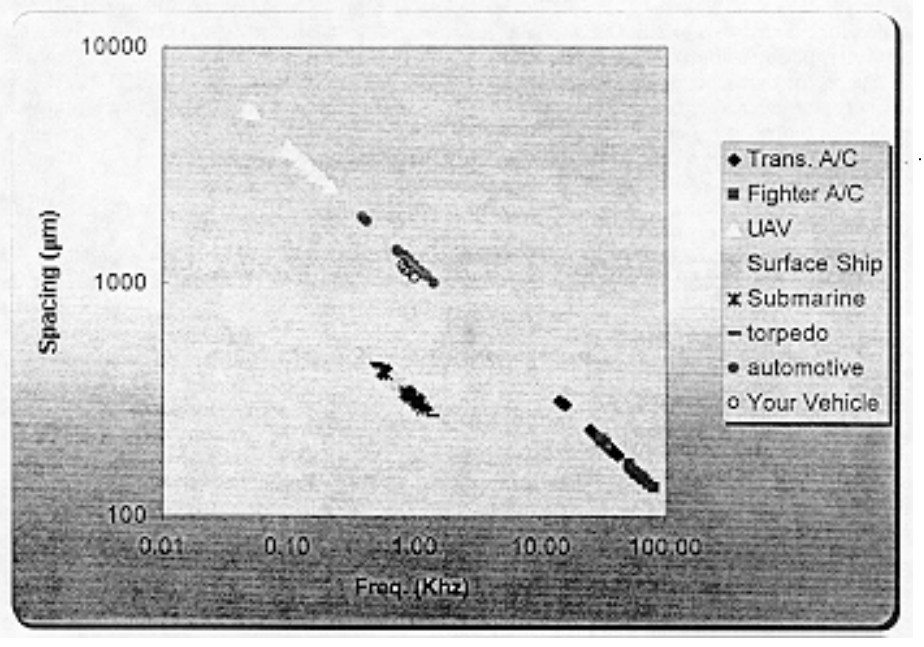

Fig. 3*a*. Microactuator spacing and frequency requirements for vehicle types in Table 1.

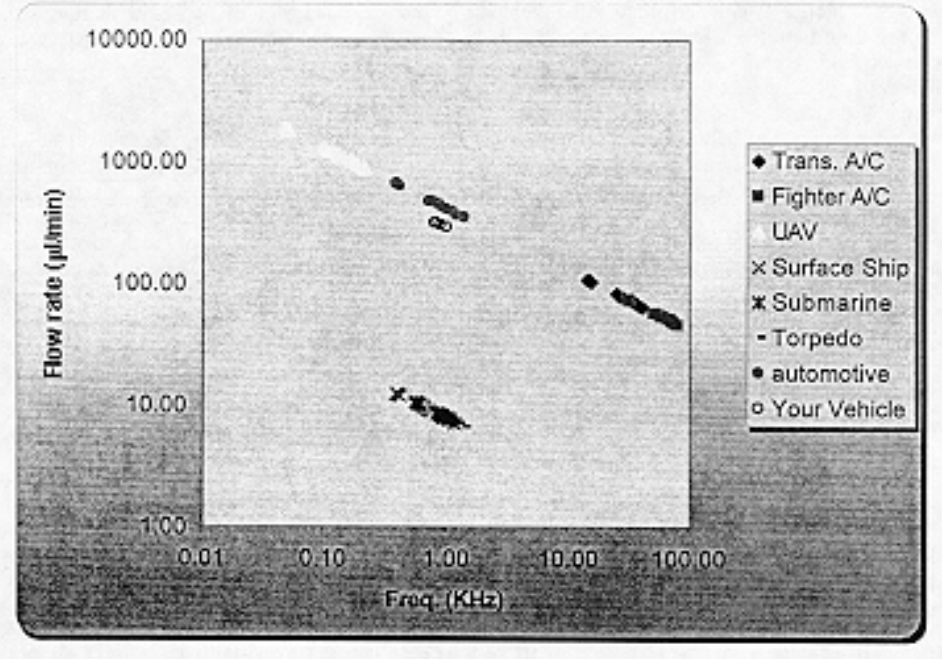

Fig. 3*b*. Equivalent DC flowrate requirements of microactuators for vehicle types in Table 1.

Figure 3. Microactuator spacing, frequency, and flowrate requirements for vehicle types in Table 1. Among aeronautical applications there is a wide range of performance requirements, depending principally on the vehicle speed. Hydronautical applications span a narrower range, and have the lowest flowrate requirements due largely to the higher fluid density.

electric field induces a drift in the mobile ions within the outer layer. This ion drift extracts energy from the applied field and transfers this kinetic energy to the bulk fluid through collisions in the thin outer layer. The bulk fluid then transfers momentum from the thin outer layer across the rest of the channel by viscous diffusion. In this manner, an applied voltage along the length of the channel produces motion of the bulk fluid within the channel.

Coulomb's law gives the electrostatic force $F = e_0 E$ acting on an ion of effective charge e_0 in an electric field of strength E. This accelerates the ions until the drag force D resulting from collisions with the surrounding solvent molecules matches the Coulomb force; the time to reach this steady state is typically $O(10^{-13}$ sec). Assuming that D can be approximated by the Stokes sphere-drag formula gives

$$D = 4\pi r \mu U \ , \tag{1}$$

where r is the equivalent spherical radius of the ion, μ is the solvent viscosity, and U is the speed at which the ion drifts, with the constant reduced to correct for the geometry. Equating gives $U = \Omega E$, where Ω is the ionic mobility

$$\Omega = \frac{e_0}{4\pi r \mu} \ . \tag{2}$$

When the field is created by an applied voltage ΔV across an actuator channel of length L and radius w, then the resulting flow speed is

$$U = \Omega \frac{\Delta V}{L} \tag{3}$$

and the volume flowrate is

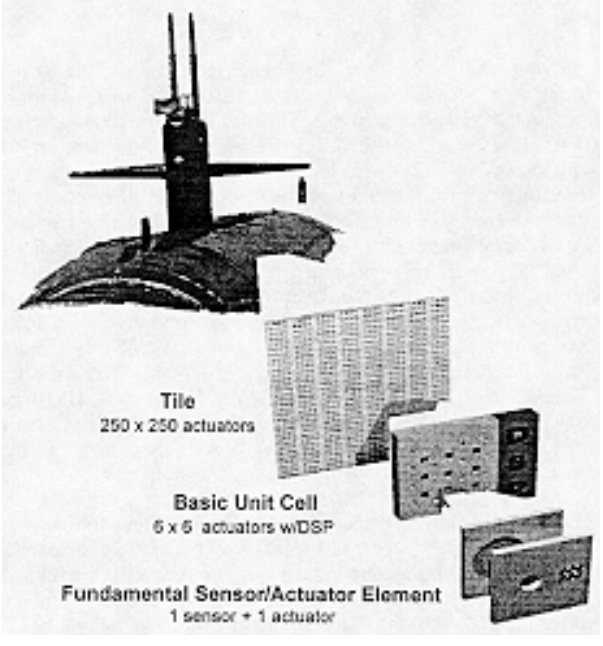

Figure 4. Schematic indicating basic architecture of point microactuator arrays in Fig. 2b for sublayer control. Locality of the sublayer vortex dynamics allows large-area microactuator tiles covering key parts of the vehicle surface to be composed of smaller "unit cells", each consisting of a typically 6 × 6 array of individually addressable microactuators with a colocated sensor array and on-board digital signal processing.

$$Q = \pi w^2 \Omega \frac{\Delta V}{L} \ . \tag{4}$$

If the actuator becomes plugged, then the pressure gain along the electrokinetic channel is balanced by the pressure drop in the backflow along the actuator. The latter is obtained from the Poiseuille flow solution as

$$\Delta p = 8\mu\Omega \frac{\Delta V}{w^2} \tag{5}$$

and hence the force achieved by the actuator channel is

$$F = 8\pi\mu\Omega\Delta V \ . \tag{6}$$

It is popular to equivalently express the mobility Ω in terms the potential ζ achieved across the inner layer (the "zeta potential" or "wall potential") as

$$\Omega = \frac{\varepsilon_0 \kappa \zeta}{\mu} \ , \tag{7}$$

where ε_0 is the permittivity constant and κ is the dielectric constant.

These scalings are for a single channel. For a channel of radius R consisting of $(R/w)^2$ individual pores each of radius w, the flow rate in (4) becomes

$$Q = \pi R^2 \Omega \frac{\Delta V}{L} \ . \tag{8}$$

Benchtop testing conducted with electrokinetic microactuators formed from capillaries packed with glass beads of size w and operated under DC conditions (see §8.1) verified that the pressure achieved increased linearly with applied voltage ΔV and varied with bead diameter (and hence effective channel radius) as w^{-2}, as suggested by (5). The volume displacement rate Q also was observed to increase linearly with applied voltage and the ionic mobility Ω as in (8).

For electrokinetic driver sections based on porous channels with extremely fine pores, the resulting pore Reynolds number Uw/ν will be very low, and thus inertial damping of the unsteady response should be negligible. Furthermore, the extremely short time scale on which the Coulomb force equilibrates with the ion drag suggests that, in the presence of a time-varying applied field, the frequency response of a microactuator based on the electrokinetic principle will be very high.

Note also in (3) that the flow speed achieved is independent of the pore radius w, but the pressure in (5) increases as the pores are made smaller. This further suggests that by fabricating electrokinetic channels with sufficiently small pores, it may be possible to achieve flowrates adequate to meet the requirements in §4 while at the same time achieving sufficiently high pressures in any plugged actuators to allow these to unplug themselves.

These considerations suggest that microactuator arrays based on the electrokinetic principle may be able to meet the requirements in §4 for sublayer control on vehicles under realistic conditions.

6. Hydrodynamic Models of Frequency Response

As noted in Fig. 3*b*, practical microactuators for sublayer control must operate at frequencies around 1 kHz for hydronautical applications, and at frequencies as high as 90 kHz for the most demanding aeronautical applications. The ultimate frequency response limits of such unsteady electrokinetic microactuators is

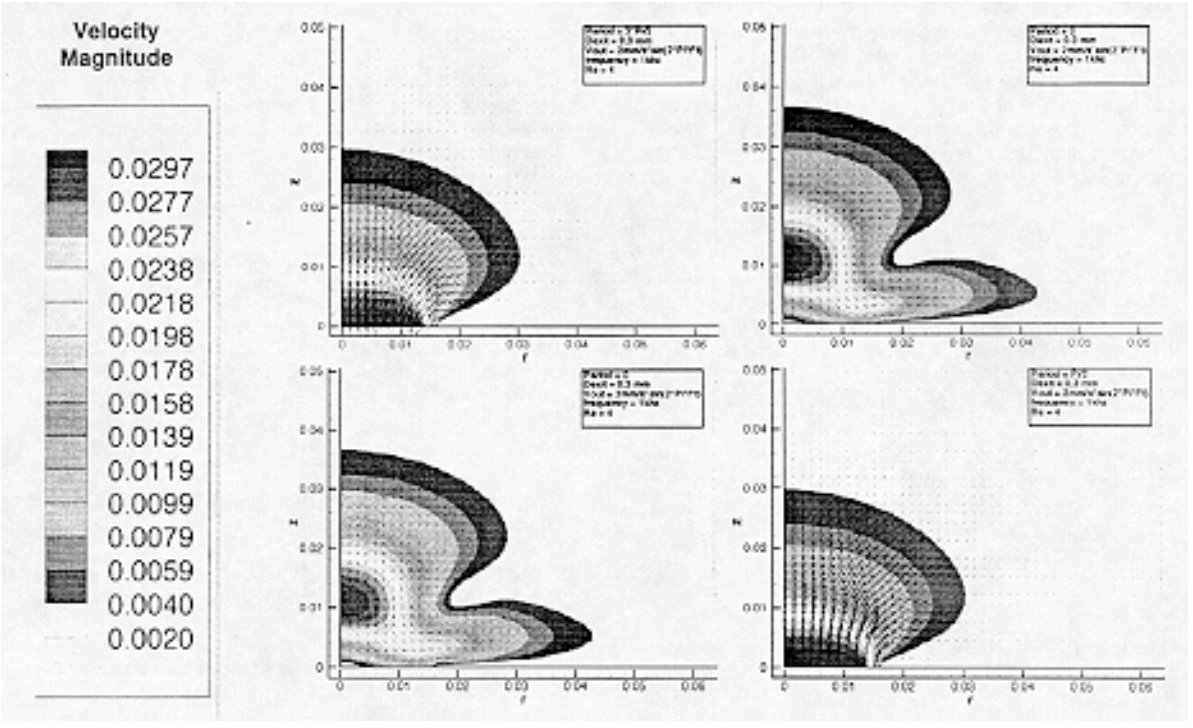

Figure 5. Full Navier-Stokes simulations of the axisymmetric flow induced by a single, 300 μm diameter microactuator of the type in Fig. 2*b* operating at 1 kHz in water with equivalent DC flowrate of 10 μl/min, typical of hydronautical applications in Fig. 3. Shown are velocity magnitude and velocity vectors over a half-period of the oscillatory driving. The flow is fully reversible at these conditions owing to the very low Reynolds number. Note also that the no-slip condition at the wall nevertheless produces roughly hemispherical displacements induced by microactuator.

unknown, however assuming that capacitances are properly managed there are two distinctly different physical processes that can limit their performance. The first is frequency response limitations in the coupling between the electric field and the ion drift in the outer layer. Relatively little information exists in the literature on unsteady electrokinetic processes, but owing to the physics associated with this process (see §5) it may be anticipated that this response limit will be considerably higher than the requirements in Fig. 3*b*.

The second limit is due to inertial damping by the flow within the electrokinetic driver matrix. In order to estimate the theoretical frequency response attainable with such electrokinetic microactuators, in this section we use simple models based on the hydrodynamics of electrokinetically driven flow to assess the potential frequency response and the key parameters that will set the response limit.

We consider the flow in a typical pore of radius w within the porous matrix of the electrokinetic driver section as indicated in the center layers in Fig. 3. The response of the pore flow to an unsteady electrokinetic forcing can be approximated by simple hydrodynamic models. Two closely related limits are relevant. The first applies when the electrokinetic double layer thickness is much smaller than the pore radius w, as is typically the case. The motion induced in the double layer by either an impulsively applied electric field, or by a sinusoidally oscillating applied field, is then equivalent, respectively, to Stokes' first or second problem for the flow induced by viscous diffusion above a moving wall. The "wall" in this case is the oscillating thin double layer, and viscosity acts to diffuse the induced motion within it throughout the pore. The solutions are classical, and in both cases lead to the development of a "Stokes layer" of thickness $\lambda \approx (\nu/2\omega)^{1/2}$ adjacent to the wall within which the motion is confined, with ν is the viscosity of the electrolyte in the pore and ω the frequency of the applied field. The frequency at which the Stokes layer becomes smaller than the pore radius is then $\omega_{max} \approx (\nu/w^2)$, beyond which diffusion has insufficient time to transfer momentum from the double layer to the rest of the pore. Assuming an aqueous electrolyte with kinematic viscosity comparable to that of water ($\nu \approx 10^{-6}$ m^2/s), this would suggest a maximum frequency of the order of 1 MHz for 1 μm pores, and 10 kHz for 10 μm pores, but drops to 400 Hz for 50 μm pores. For the porous polymer matrix used to fabricate the arrays in §8, the average pore size is roughly 1 μm, and this would suggest frequency response up to around 1 MHz.

The second limit applies when the double layer thickness is greater than the pore radius, in which case the electrolyte throughout the pore contains a largely uniform concentration of ions. The electrokinetic forcing then acts to induce motion directly throughout the fluid and thereby becomes equivalent to a body force. This is equivalent to the oscillatory flow induced in a pipe by a sinusoidally varying pressure gradient. This limit also has an exact solution (by Sexl 1930) that is classical and can be used to assess frequency response limits applicable to that case. However for the double layer thicknesses encountered to date in our work, this does not appear to be the limiting case.

These simple considerations suggest that it should be possible to meet the frequency response requirements in Fig. 3*b* for all vehicle types shown with microactuators having a typically 1 μm porous matrix in the electrokinetic channels in Fig. 2.

7. Numerical Simulations of Actuator Displacement

Owing to their exceeding small size, the flow issuing from each microactuators is at low Reynolds number. Consequently viscous diffusion is the dominant transport mechanism, and thus streamlines of the induced flow field will be nearly reversible. However, the simple hemispherical displacement indicated in Fig. 1 is a highly idealized representation of the actual flow induced by an individual microactuator. The viscous no-slip condition at the wall prevents the flow from inducing any displacement directly at the wall, and limits the induced displacement for some distance above the wall. Numerical simulations were conducted to determine if this would prevent the actuator from inducing sufficient radial outward motion to adequately displace the sublayer vortical structures.

The axisymmetric, incompressible Navier-Stokes equations were solved for the velocity field $\mathbf{u}(\mathbf{x},t)$ induced by a single microactuator issuing into a quiescent fluid. The simulations are thus intended only to address the effects of the no-slip condition, and do not address the "streaming" effect created by the interaction between the microactuator-induced flow and the streamwise flow within the inner layer. A staggered 66 × 130 computational grid spanned a 1.2 mm × 2.4 mm axisymmetric half-domain. Axisymmetry was imposed at the left (centerline) boundary, with outflow boundaries imposed on the right and top. The bottom boundary consisted of a no-slip wall with uniform oscillatory inflow through a 150 μm radius actuator nozzle. The inflow varied sinusoidally with 1 kHz frequency and peak velocity of 2.85 mm/sec. Advection terms were discretized using the QUICK scheme and diffusion terms with a second-order centered scheme. First-order explicit time integration was used. A projection method was used for the Navier-Stokes equations, with the pressure field obtained from a Poisson equation by a multigrid method. Fluid properties were set to water values.

Results for the induced flow are shown over a half-period of motion in Fig. 5. At the peak of the outflow phase (bottom right panel) the effect of the no-slip condition at the wall is evident, however there is adequate radial displacement within 50 μm above the wall. Throughout the rest of the actuation cycle as well, the flow provides sufficient radial displacement except very close to the wall. It is concluded that the effect of the no-slip requirement at the wall under these conditions will not interfere with the required microactuator flow.

8. Microactuator Fabrication and Testing

Several early actuator arrays were fabricated and used to test various aspects of electrokinetic microactuator performance as well as to develop practical mass fabrication approaches. These have evolved the design from initial tests with elementary packed channel actuators, to small arrays of fully functioning microactuators, to unit cell sized components (see Fig. 4).

8.1. *Elementary Packed Channel Actuators*

Initial tests were done with simple capillaries packed with glass beads of various diameters to verify the scaling principles relevant to electrokinetic pumping under steady (DC) applied fields. The scalings in §4 were confirmed experimentally in tests using 100 μm glass capillaries filled with various electrolytes. These showed that miniaturization by constructing additional interfacial surface (and hence additional double layer area) within the channel interior allows large increases in pressure rise Δp to be achieved in plugged actuators while causing essentially no reduction in volume displacement rate Q for open actuators. This was accomplished by filling the actuators with glass spheres having diameters as small as 0.5 μm, creating effective interstitial channels with submicron scales. The dependence of pressure rise and flowrate on the applied voltage ΔV and channel length L were also verified. The performance advantages of miniaturization should continue to apply down to the Debye length scale. Further tests verified the dependence of performance on electrolyte type and concentration as suggested by the ionic mobility in (7).

8.2. *"Mod 0" 3 × 3 Microactuator Array*

Based on the results from experiments with elementary packed channel actuators, the initial 3 × 3 microactuator array in Fig. 6 was fabricated and used for testing. This array is somewhat smaller than the typical 6 × 6 unit cell in Fig. 4, but sufficed for an initial exploration of the major challenges involved in unit cell fabrication, and for initial performance testing of unsteady (AC) electrokinetic driving. For simplicity the array was sized to the requirements of a UAV-scale application in Fig. 3, and hence consisted of individual microactuators with 1000 μm diameter and 2000 μm center-to-center spacing. The basic three-layer design in Fig. 2*b* was used, with electrokinetic driver channels in the center layer and an electrolyte reservoir in the bottom layer.

The electrokinetic driver channels were in this case mechanically drilled into a 3 mm thick glass substrate. This was intended as a preliminary process used for this initial fabrication only, and not intended to represent a fabrication process suitable for eventual mass production. The substrate thickness determines the actuator length-to-diameter ratio, which must be kept large enough (L/D > 3) to maintain reasonably straight field lines within the channel.

A ring electrode was formed around the periphery of each of the microactuator channels using standard metallization and photoetching techniques. Due to chipping that occurred in the channel drilling process (*e.g.*, see Fig. 6*b*), the resulting edge quality was relatively poor. This caused some difficulties in maintaining electrode continuity on the top surface of the center layer. However, as the top two panels in Fig. 6*b* show, the resulting ring electrodes were of acceptable quality. Leadouts from the individual channels are also visible in Fig. 6. The bottom surface electrode is the common for all the channels, and can be seen in the bottom two panels in Fig. 6*b*.

The glass beads used in the initial benchtop tests in §8.1 were replaced by a technique for producing a porous polymer matrix in the electrokinetic driver channels. This technique uses a gel consisting of several constituents, including butyl methacrylate with a solvent and with a dopant to provide the zeta potential, that could be readily introduced into the channels. The center layer was subsequently baked at 40-60 °C over several hours to yield the porous polymer matrix in the channel, producing $O(1\ \mu\text{m})$ diameter pores throughout the channel. The porous polymer matrix is visible as the white material in the channels in Fig. 6*a*. Filling of the porous polymer with electrolyte was readily accomplished by simply applying a DC voltage across the top and bottom surface electrodes for each channel. The electrolyte quickly wetted the entire channel and flowed from the top of each actuator.

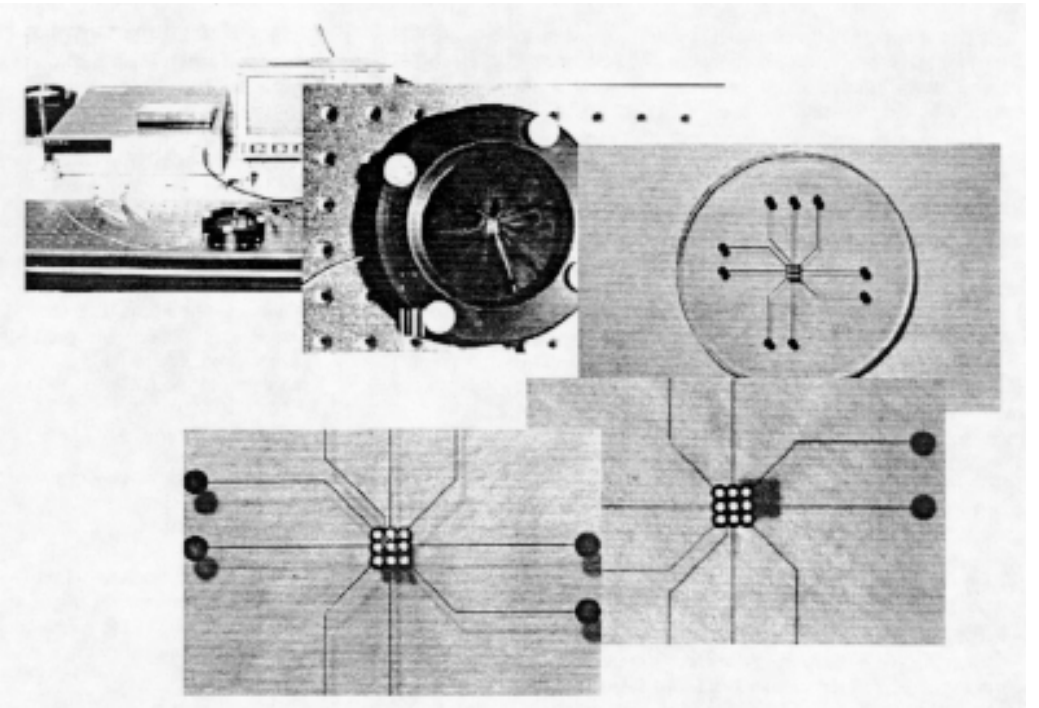

Fig.6*a*. Successively zoomed views of "Mod 0" array in glass, showing test apparatus, leadouts, and top and bottom surfaces.

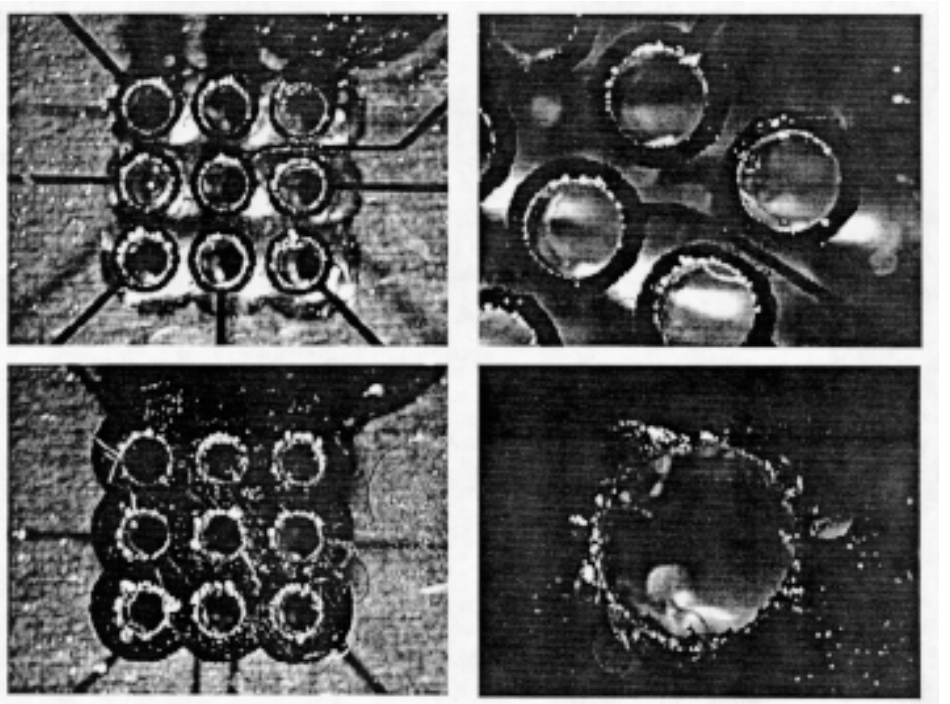

Fig.6*b*. Photomicroscope views of surface metallization and electrodes showing edge imperfections from drilling in glass.

Figure 6. "Mod 0" 3 × 3 microactuator array fabricated in glass and used for initial testing. Individual actuators are 1000 μm in diameter and filled with porous silicon matrix having approximately 1μm pore size. Top and bottom surface metallization and leadouts are also visible. Comparison of actuator channels fabricated by mechanical and laser drilling in glass is shown in Fig. 8.

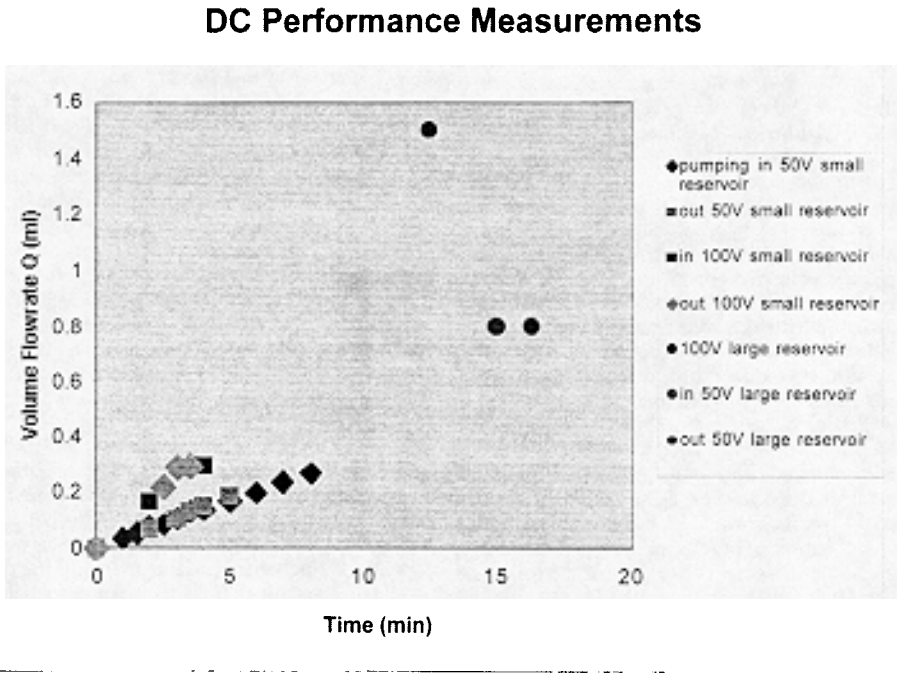

Fig.7*a*. Measured DC flowrate, showing results for two different drive voltages.

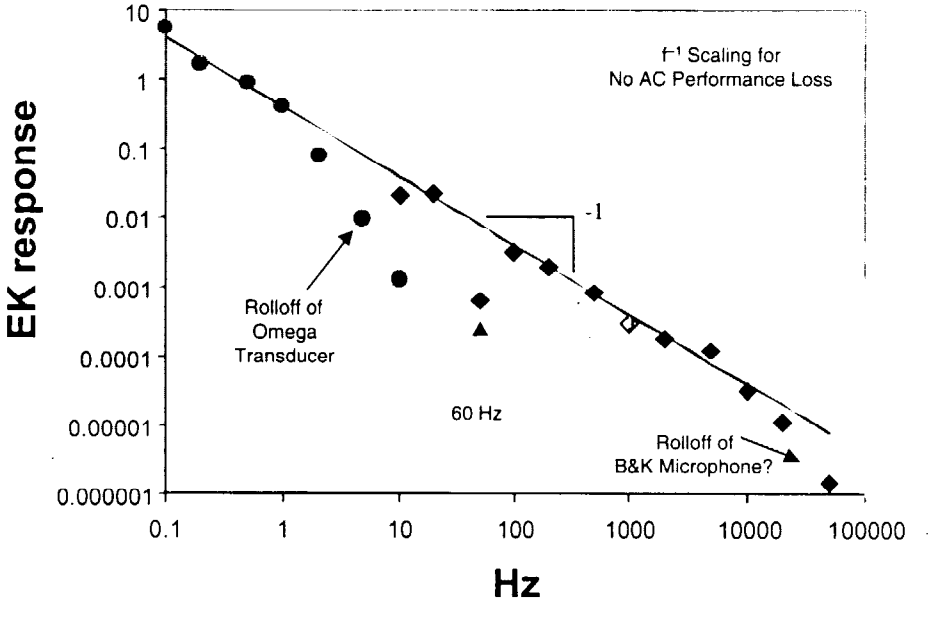

Fig.7*b*. Measured frequency response, showing comparison with theoretical f^{-1} rolloff for loss-less AC performance.

Figure 7. Measured DC and AC performance of a single "Mod 0 -type microactuator.

DC performance testing was conducted by applying steady voltage differences ΔV across the electrodes and measuring the volume flowrate over an extended time. Results are shown in Fig. 7*a*. The volume flow rate achieved was proportional to the applied voltage, consistent with (8), and for these conditions provided 0.1 μl/min at 33 V/mm.

AC performance testing was conducted to determine frequency response, by applying sinusoidally varying voltage differences. In this case, the microactuator drove a small closed cavity containing an air bubble. A pressure transducer (at low frequencies) or a microphone (at high frequencies) measured the time-varying pressure in the cavity as the air bubble was compressed by electrolyte flowing into or out of the cavity. Results are shown in Fig. 7*b*, giving the peak-to-peak signal from the transducer or microphone normalized by the manufacturer's response calibration. The f^{-1} scaling shown by the solid line is the theoretical result corresponding to loss-less AC performance; *i.e.*, the reduction in volume displacement per cycle resulting solely from the f^{-1} reduction in cycle period with frequency. The equivalent DC flow rate is thus unchanged to at least 10 kHz. This would be consistent with the onset of inertial damping within a porous matrix with 10 μm pores based considerations in §6. The origins of the rolloff above 10 kHz are presently not clear, and may be due to an experimental limitation. It is also possible that, while the pore size in the present matrix is nominally 1 μm, the largest pores may be as large as 10 μm, and that these determine the inertial damping limit for the actuator. Irrespective of these considerations, the 10 kHz frequency response demonstrated in these tests meets the demands for most of the vehicles in Fig. 3 and far exceeds the requirements for all the hydronautical applications.

8.3. *"Mod 1" 10 × 10 Microactuator Array*

Based on the performance seen with the "Mod 0" microactuator array in §8.2, a "Mod 1" array was fabricated to *(i)* assess laser drilling of the electrokinetic channels as an alternative to mechanical drilling, and *(ii)* explore design issues associated with larger unit cells. Like the "Mod 0" array, this 10 × 10 array was fabricated in glass and sized for UAV-scale applications. Individual electrokinetic channels were 2000 μm in diameter and had 5 mm center-to-center spacing.
Drilling of the electrokinetic driver channels in glass was done with a CO_2 laser by a commercial vendor. This fabrication process is amenable to eventual mass production. Comparisons of the resulting edge quality with that of the mechanically drilled holes in §8.1 are shown in Fig. 8. Edge quality achieved at this scale with laser drilling is excellent, and more than adequate for metallization and electrode etching.

The electrode layout for this 10 × 10 array is shown in Fig. 9*a*. The size is considerably larger than the anticipated 6 × 6 unit cell yet shows that electrode leadouts can be readily accommodated. Like the "Mod 0" array, the bottom surface electrode is common for all channels. The channels were filled with the same porous polymer matrix as for the "Mod 0" array. Figure 9*b* shows the resulting filled microactuator channels, where the porous matrix again appears white.

8.4. *"Mod 2" 3 × 3 Microactuator Array*

In view of the excellent edge quality achieved by the laser drilling process in the UAV-scale "Mod 1" array, the process was applied to develop a hydronautical-scale "Mod 2" array. This array consisted of a 3 × 3 matrix of electrokinetic driver

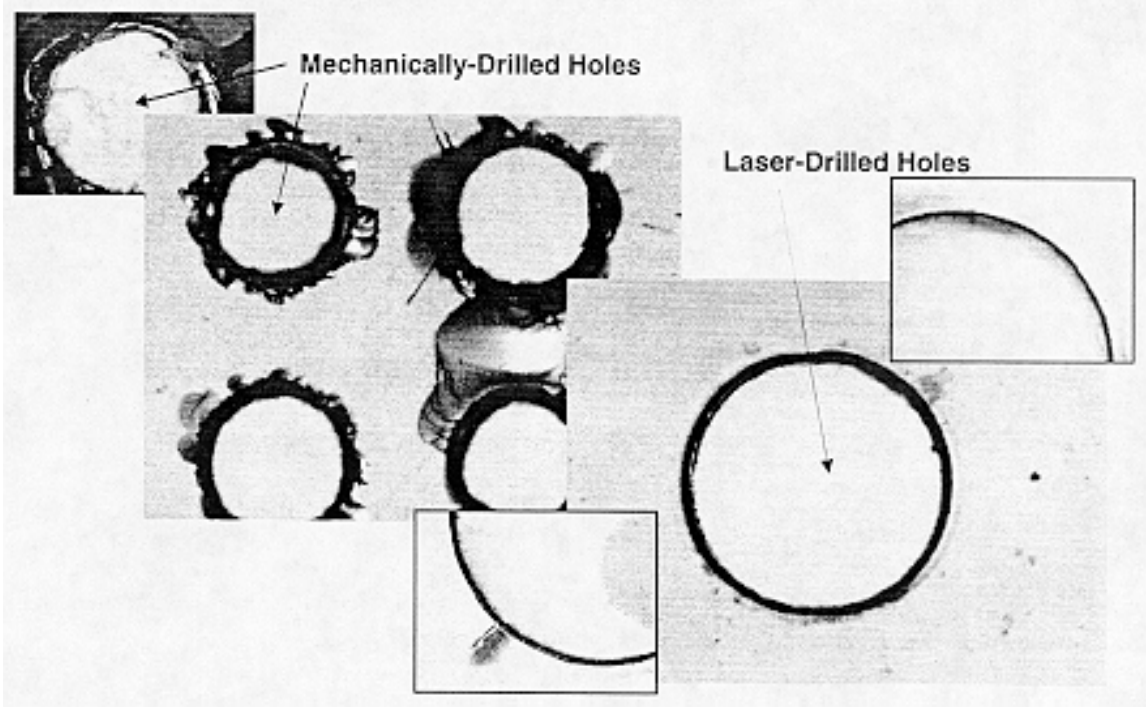

Figure 8. Comparison of edge quality for microactuator channels drilled in glass via mechanical drilling as in "Mod 0" array, and via laser drilling as in "Mod 1" array. Center layer with microactuator channels for "Mod 1" 10 × 10 array is shown Fig. 9.

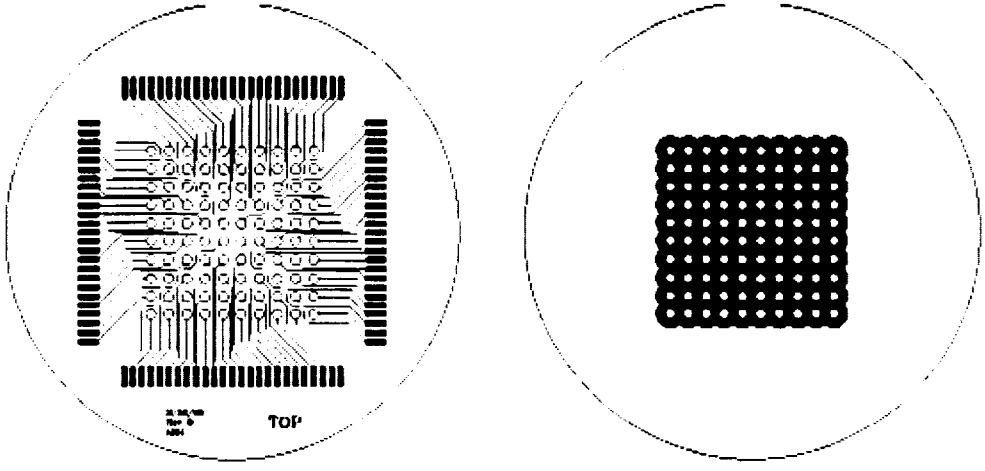

Fig.9*a*. Basic layout of center layer for "Mod 1" 10 × 10 microactuator array.

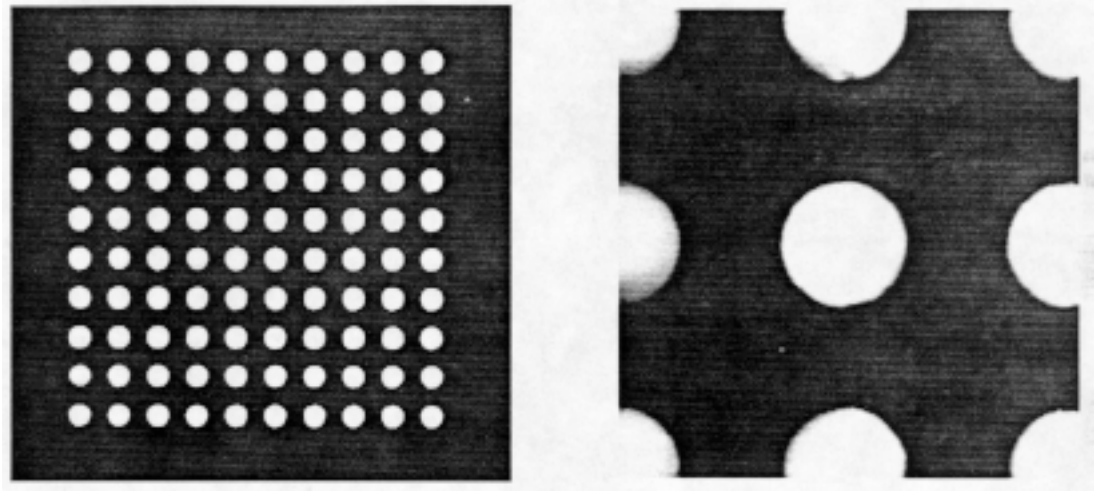

Fig.9*b*. Photographs of polygel-filled channels for "Mod 1" 10 × 10 microactuator array, showing edge quality.

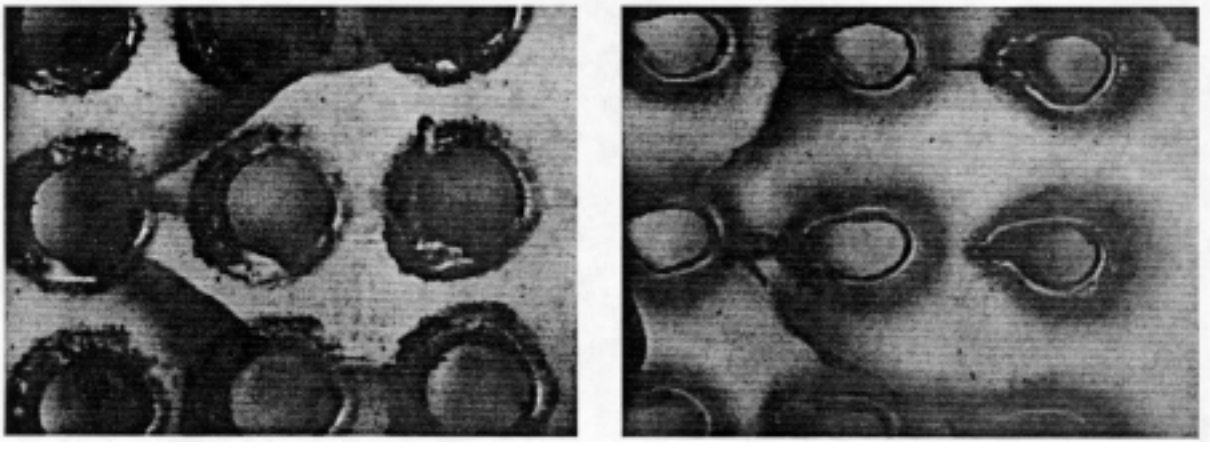

Fig.9*c*. Photographs of poor hole quality by laser drilling of 100 μm channels in "Mod 2" 3 × 3 microactuator array in glass.

Figure 9. Microactuator channels produced by laser drilling in glass, showing relatively good edge quality for 2000 μm diameter channels in UAV-scale "Mod 1" 10 × 10 array in Figs. 9*a,b*, but poor quality for 100 μm diameter channels in "Mod 2" 3 × 3 microactuator array in Fig. 9*c*.

channels, each 100 μm in diameter and 2 mm long, and with 200 μm center-to-center spacing. As with the "Mod 0" and "Mod 1" arrays, fabrication was in glass using the same CO_2 laser drilling process.

The smaller channel diameters, however, produced much poorer results from laser drilling than was the case for the 2000 μm diameter channels in the "Mod 1" array. Top and bottom surface views of the center layer for the "Mod 2" array are shown in Fig. 9*c*. These difficulties were driven by fabrication in the glass substrate. Since this was never intended as a final substrate material, subsequent arrays were fabricated with other substrate materials.

8.5. *"Mod 3" 5 × 5 Microactuator Array*

The laser drilling process was adapted for a "Mod 3" array by changing the substrate material to acrylic, which is readily amenable to laser drilling. The array, shown in Fig. 10, consisted of a 5 × 5 matrix of electrokinetic driver channels, each 300 μm in diameter and 2 mm long, and with 1000 μm center-to-center spacing. Fabrication was by the same commercial vendor using the same CO_2 laser drilling process.

Figure 11 shows close-up views of the hole quality resulting on the exit side from laser drilling at this scale in acrylic. Edge quality was generally excellent and more than adequate for metallization. There is indication of melt flow around the periphery of the hole, with further indications of a circumferential instability in the melt flow, but these do not compromise the hole quality needed for metallization such as was done in the "Mod 0" array.

Figure 12 shows much poorer edge quality on the entry side of the acrylic. The degradation appears due to cratering created by ejection of molten material from the hole, as well as melt flow along the surface. However, since only one side of the center layer needs to be metallized, this can be done on the entry side, where edge quality is higher.

The results obtained from this "Mod 3" fabrication with laser drilling in acrylic do suggest, however, that it may be possible to mass produce the center layer in thin plastic films by such a process. The porous polymer can be readily wiped into the channels, and baking to form the porous matrix is at temperatures compatible with these materials. However, acrylic is unsuitable as a substrate since it is incompatible with the solvents used in the polygel process. There are other plastics that can be readily laser drilled and that are compatible with the polygel process. Current work on fabrication and testing of "point" microactuator arrays is working with such materials.

8.6. *"Mod 4" 10 × 1 Slot Microactuator Array*

In view of the potential simplicity offered by open-loop control of the sublayer vortices using the "oscillating wall" approach in §3, an initial "slot" microactuator array of the type in Fig. 2*a* was developed. Unlike the "point" microactuator arrays, for which the spacing between individual microactuators must be comparable to the 100 l_τ sublayer vortex separation, the slot arrays seek to manipulate large numbers of sublayer vortices between adjacent slots, and thus can be spaced much farther apart. Elementary considerations suggest that, to first order, the effectiveness of the slot actuators in oscillating the fluid above the wall is independent of how large the slot spacing is made.

The same basic three-layer design is used for slot arrays. To examine issues associated with design and fabrication of such slot microactuator arrays, the top layer of the initial "Mod 4" array consisted of a 10 × 1 array of 500 μm wide slots, each 2 cm long and with 5 mm spacing between adjacent slots. The center layer consisted of much larger electrokinetic driver "beds" centered below each slot, into which the porous polymer matrix would be filled. These layers are shown in Fig. 13.

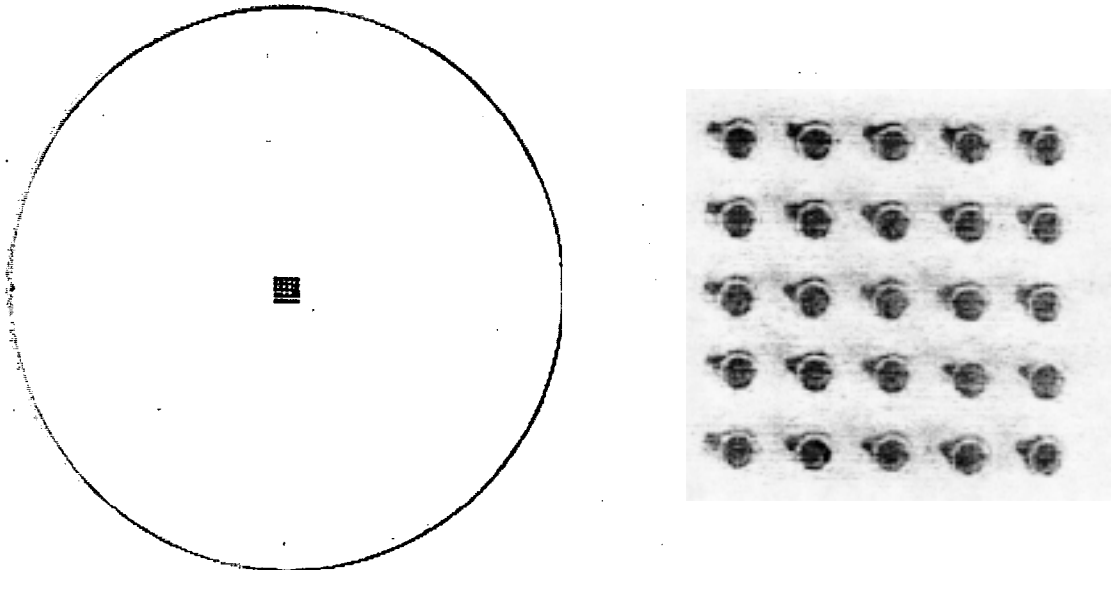

Figure 10. Microactuator channels for "Mod 3" 5 × 5 array with 300 μm diameter channels produced by laser drilling in acrylic, yielding relatively good edge quality on exit side as can be seen in Figs. 11. Laser drilling also allows rapid fabrication of large arrays microactuator channels.

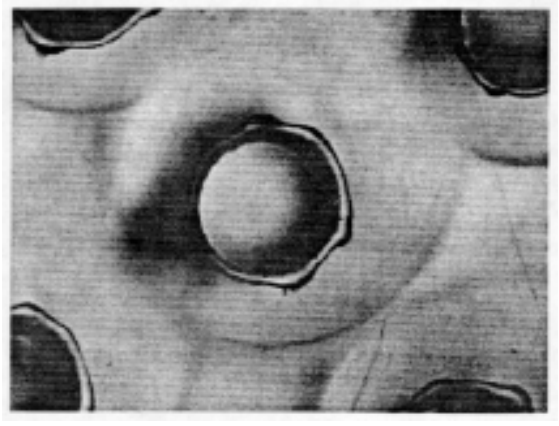

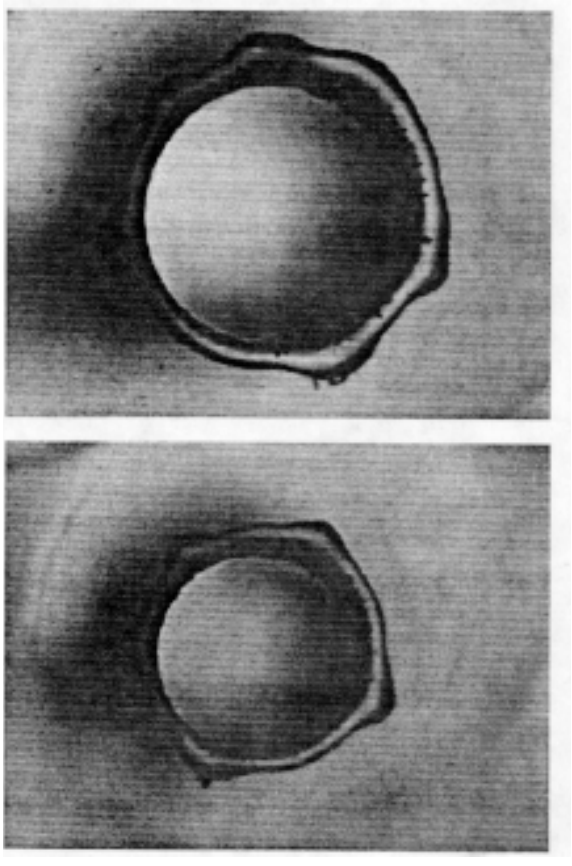

Figure 11. Photographs of microchannel quality produced by laser drilling of 300 μm channels in acrylic center layer of "Mod 3" 5 × 5 microactuator array in Fig. 10. Edge shows indications of circumferential instability in melt flow, but resulting surface quality is adequate for metallization.

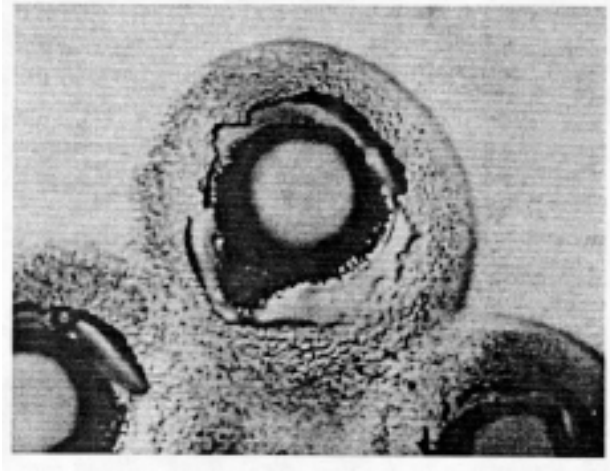

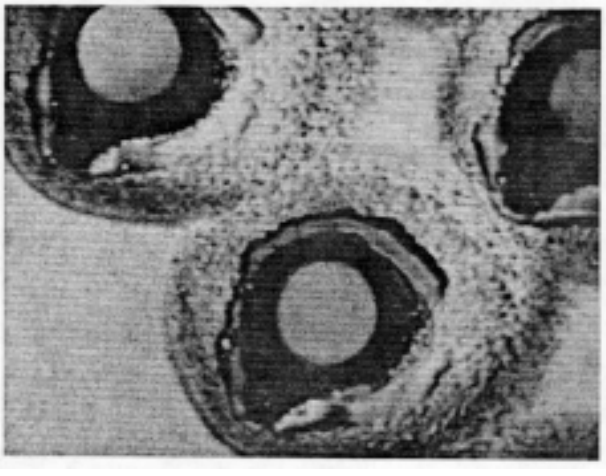

Figure 12. Photographs showing relatively poor quality of surface around microchannel periphery produced on entry side by laser drilling of 300 μm channels in "Mod 3" array in acrylic. Cratering is due to material ejection on entry side in laser drilling process. However, metallization is needed on only one side of the center layer, and can thus be done on exit side shown in Fig. 11.

As with the "Mod 3" array in §8.5, fabrication of the top and center layer blanks was readily done by laser drilling in acrylic. Figure 14 shows the resulting edges in both layers. Similar instabilities in the melt flow at the edges of the slots are evident in Fig. 14*a*, but these would in no way compromise electrode deposition. Current work on slot arrays is using other materials that are compatible with the solvents in the polygel, and will allow assembly of a complete slot microactuator array similar as was done for the "Mod 0" point microactuator array.

9. Concluding Remarks

The present paper has documented basic principles relevant to closed-loop and open-loop control of streamwise vortical structures in the viscous sublayer of turbulent boundary layers for drag reduction on vehicles, and demonstrated that the electrokinetic principle can provide the basis for a class of microactuator arrays to control the sublayer vortices. "Point" microactuators of the type in Fig. 2*b* serve as volume sources to impulsively displace the sublayer vortices as indicated schematically in Fig. 1 so as to interrupt the interaction between adjacent structures and thereby delay or defeat the bursting process. "Slot" microactuators of the type in Fig. 2*a* also serve as volume sources, but operate in an oscillatory manner with alternating slots in opposite phases so as to introduce spanwise oscillations in the fluid above the wall. Performance requirements for such microactuator arrays at various locations on different types of aeronautical and hydronautical vehicles were given in Fig. 3. A basic architecture comprised of small, independent unit cells with local sensing and signal processing is appropriate for closed-loop control with point microactuator arrays. For the slot arrays, no local sensing or processing is required. Fundamental considerations related to the physics of the electrokinetic process indicate the basic scaling laws that govern such microactuators. These show advantages obtained from miniaturization of the electrokinetic channels by use of a porous matrix with μm-scale pores in the center layer of the proposed three-layer design. Simple hydrodynamic models for the electrokinetically-driven flow in such a porous matrix suggest that inertial damping should remain irrelevant up to frequencies approaching 1 MHz. Simulations of the flow induced by such an actuator indicate that the no-slip condition at the wall will not interfere significantly with the radial outflow needed to displace the sublayer streaks in the case of point actuators.

Several microactuator arrays or components have been assembled to study various aspects of the performance and fabrication processes relevant to electrokinetic microactuator arrays. The "Mod 0" array in §8.2 consisted of an individually addressable 3×3 array that demonstrated good DC and AC performance, with essentially loss-less AC performance seen to at least 10 kHz. Other actuator components have been built for point array sizes up to 10×10 unit cells, and microactuator diameters as small as 100 μm with center-to-center spacings as small as 200 μm. The porous polymer matrix proved to allow relatively easy fabrication of μm-scale electrokinetic channels. Laser drilling proved to be a practical means for fabricating the channels in the substrate material. Standard metallization and photoetching allowed ring electrodes and associated leadouts, as well as common electrodes, to be fabricated on the center layer.

Microactuator arrays based on the electrokinetic process are robust, they have no moving parts, they can achieve high frequency response, and they can achieve high pressures when individual actuators are blocked. All of these attributes serve to make such actuators potentially suitable for practical sublayer control on real vehicles.

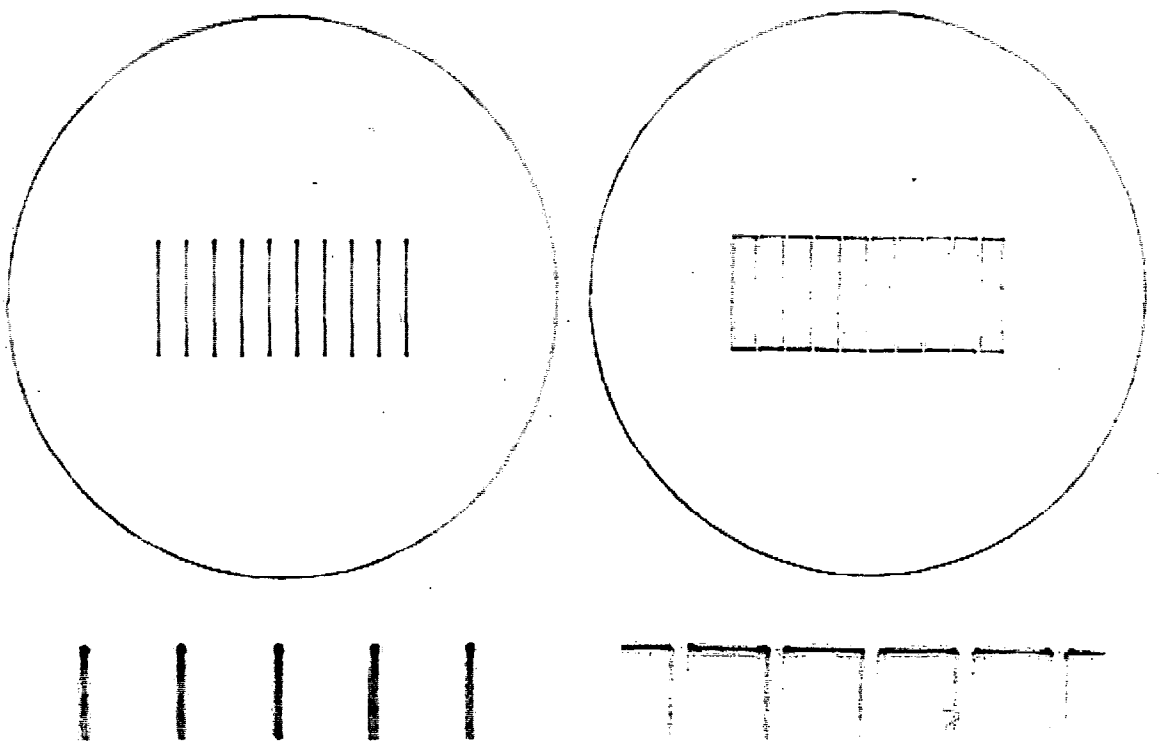

Figure 13. Microactuator channels and slot nozzles for "Mod 4" 10×1 slot array produced by laser drilling in acrylic. Edge quality is shown in Fig. 14.

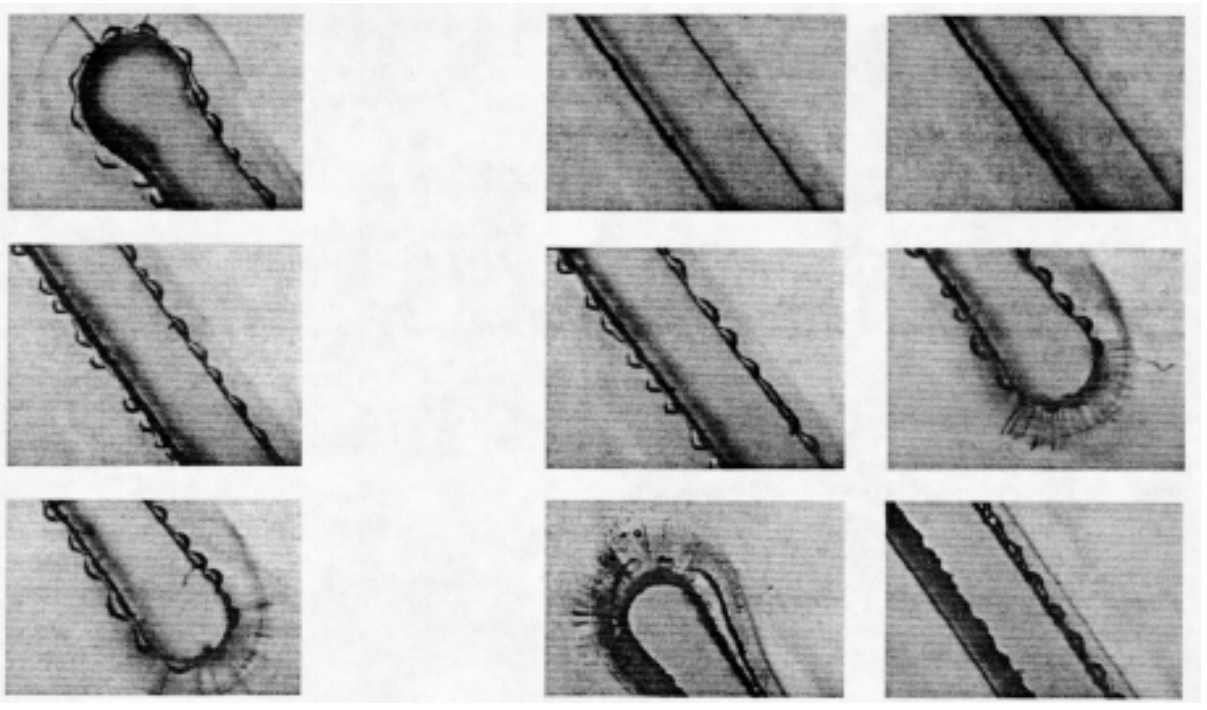

Fig.14*a*. Photographs of 300 μm slot nozzles in top layer of "Mod 4" 10 × 1 microactuator array, showing edge quality.

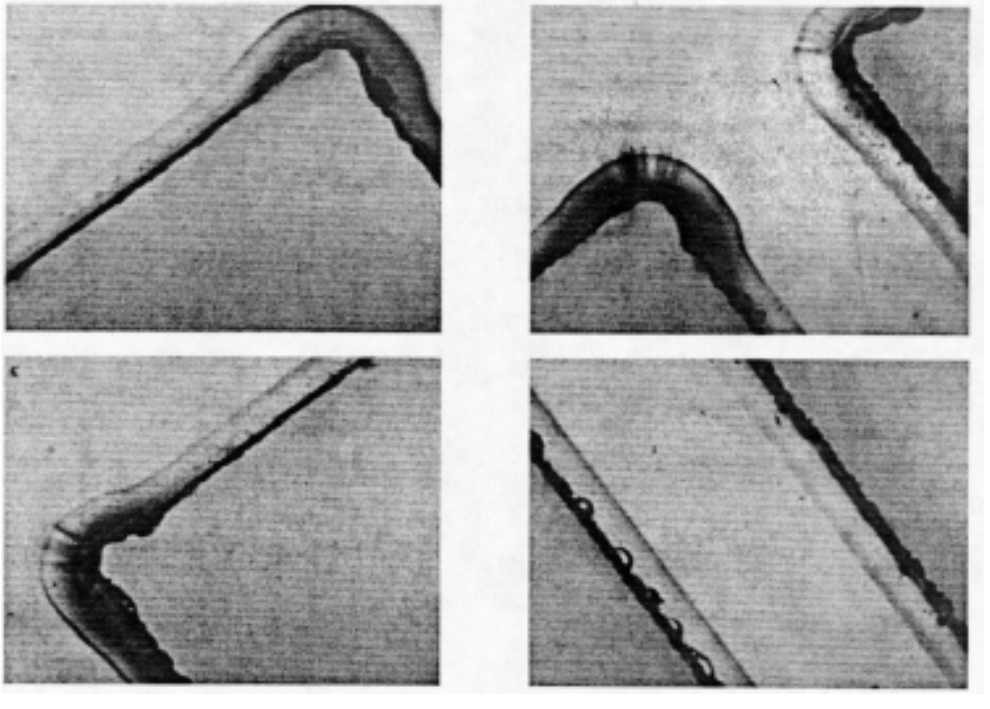

Fig.14*b*. Photographs of microactuator channels in center layer of "Mod 4" slot array.

Figure 14. Microactuator channels and slot nozzles produced by laser drilling in acrylic for "Mod 4" 10 × 1 slot array in Fig. 13.

Acknowledgements

This work is supported by the Defense Advanced Research Projects Agency (DARPA) Microsystems Technology Office (MTO) under Contract No. F30602-98-2-0228 at The University of Michigan. The technical assistance of Mr. Ken Hencken at Sandia National Laboratories in fabrication and testing of the electrokinetic microactuators is gratefully acknowledged. The code used for the numerical simulations was provided by Prof. Grétar Tryggvason of The University of Michgian.

References

Akhavan, R., Jung, W.J. & Mangiavacchi, N. (1992) Turbulence control in wall bounded flows by spanwise oscillations. *Appl. Sci. Res.* **51**, 299-303.

Breuer, K.S., Haritonidis, J.H. & Landahl, M. (1989) The control of transient disturbances in a flat plate boundary layer through active wall motion. *Phys. Fluids A* **1**, 574-582.

Bushnell, D. & McGinley, C. (1989) Turbulent control in wall flows. *Annu. Rev. Fluid Mech.* **21**, 1-20.

Choi, H., Moin, P. & Kim, J. (1994) Active turbulence control for drag reduction in wall-bounded flows. *J. Fluid Mech.* **262**, 75-110.

Coles, D. (1956) The law of the wake in the turbulent boundary layer. *J. Fluid Mech.* **1**, 191.

Dahm, W.J.A., Paul, P.H., Rakestraw, D.J. and Scherer, J.J. (1997) Fluid microactuators based on the electrokinetic principle. Bulletin of the American Physical Society, Vol. 42 (11), p. 2247.

Fiedler, H.E. & Fernholz, H.H. (1990) On management and control of turbulent shear flows. *Prog. Aerospace Sci.* **27**, 305-387.

Gad-el-Hak, M. (1989) Flow control. *Appl. Mech. Rev.* **42**, 261-293.

Gad-el-Hak, M. (1994) Interactive control of turbulent boundary layers: A futuristic overview. *AIAA J.* **32**, 1753-1765.

Gad-el-Hak, M. (1996) Modern developments in flow control. *Appl. Mech. Rev.* **49**, 365-379.

Ho, C.-M. & Tai, Y.-C. (1996) Review: MEMS and its application to flow control. *J. Fluids Engng.* **118**, 437-447.

Ho, C.-M. & Tai, Y.-C. (1998) Micro-electro-mechanical-systems (MEMS) and fluid flows. *Annu. Rev. Fluid Mech.* **30**, 579-612.

Jacobson, S.A. & Reynolds, W.C. (1998) Active control of streamwise vortices and streaks in boundary layers. *J. Fluid Mech.* **360**, 179-211.

Jung, W.J., Mangiavacchi, N. & Akhavan, R. (1992) Suppression of turbulence in wall-bounded flows by high-frequency spanwise oscillations. *Phys. Fluids A* **4**, 1605-1607.

Laadhari, F., Skandaji, L. & Morel, R. (1994) Turbulence reduction in a boundary layer by a local spanwise oscillating surface. *Phys. Fluids* **6**, 3218-3220.

Löfdahl, L. & Gad-el-Hak, M. (1999) MEMS applications in turbulence and flow control. *Prog. Aerospace Sci.* **35**, 101-203.

Lumley, J.L. & Blossey, P. (1998) Control of turbulence. *Annu. Rev. Fluid Mech.* **30**, 311-327.

McMichael, J.M. (1996) Progress and prospects for active flow control using microfabricated electromechanical systems (MEMS). *AIAA Paper 96-0306*, AIAA, Washington, D.C.

Moin, P. & Bewley, T. (1994) Feedback control of turbulence. *Appl. Mech. Rev.* **47**, S3-S13.

Pollard, A. (1998) Passive and active control of near-wall turbulence. *Prog. Aerospace Sci.* **33**, 689-708.

Wilkinson, S.P. (1990) Interactive wall turbulence control. In Viscous Drag Reduction in Boundary Layers (Bushnell, D.M. & Hefner, J.N., Eds.) *Prog. Astronautics & Aeronautics* **123**, 479-509, AIAA, Washington, D.C.